# On the potential of Resonant Ultrasound Spectroscopy applied to the non-destructive characterization of the density of (LPBF) additively manufactured materials

Florian Le Bourdais, Jitendra Singh Rathore, Camille Ly, Michel Pellat, Caroline Vienne, Vincent Bonnefoy, Vincent Bergeaud, Jean-Paul Garandet

Additive Manufacturing 58 (2022) 103037

Contents lists available at ScienceDirect

Additive Manufacturing

journal homepage: www.elsevier.com/locate/addma

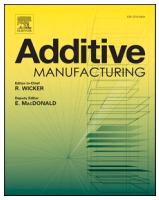

# On the potential of Resonant Ultrasound Spectroscopy applied to the non-destructive characterization of the density of (LPBF) additively manufactured materials

Florian Le Bourdais [a,*], Jitendra Singh Rathore [a], Camille Ly [a], Michel Pellat [b], Caroline Vienne [a], Vincent Bonnefoy [b], Vincent Bergeaud [a], Jean-Paul Garandet [a,b]

[a] Université Paris-Saclay, CEA, List, Palaiseau, France
[b] Université Grenoble Alpes, CEA LITEN, Grenoble, France

ARTICLE INFO

*Keywords:*
Resonant ultrasound spectroscopy
Laser powder bed fusion
Nondestructive testing, Archimedes density measurement
X-ray computed tomography

ABSTRACT

The objective of the present work is to investigate the potential of Resonant Ultrasound Spectroscopy (RUS) as an innovative technique for the nondestructive analysis of Laser Powder Bed Fusion (LPBF) $AlSi_7Mg_{0.6}$ parts. The acoustic resonance measurements are tested against an experimental database that covers a broad range of process parameters and large variations of the standard volumetric energy density. Two other nondestructive techniques are used to assess the potential of the RUS measurements of additively manufactured samples: the easy-to-use Archimedes density measurement and the cost-intensive computerized X-ray tomography. Our results show that RUS provides both qualitative and quantitative insights that allow the detection of the amount of lack of fusion porosities and the estimation of the elastic properties of the fabricated samples. Quantitative correlations between the three nondestructive testing methods are obtained, hinting at how RUS could be used effectively for systematic post-production testing of LPBF samples.

## 1. Introduction

Among the various Additive Manufacturing (AM) technologies, Laser Powder Bed Fusion (LPBF) has the potential of becoming a game changer in the way industry manufactures net shape or near net shape parts for demanding applications, e.g. in the medical, energy or aerospace sectors. However, the requirements in terms of part quality are of course much more stringent than for mere prototyping. In this respect, Non Destructive Testing (NDT) techniques have a key role in the characterization of materials that often present quite different solidification microstructures with respect to those coming from more conventional fabrication methods, such as foundry or welding.

Regarding one of the most important material properties, namely the density of the fabricated parts, comparison between a number of standard techniques have already been discussed in the AM literature [1,2]. The a priori simplest and most obvious method is to realize various cuts within the material to be tested, and to perform metallographic analyses on these cuts. With a suitable polishing taking due care of smearing issues, porosities can be detected and analyzed in terms of distribution thanks to automated image analyses procedures [3]. However, the technique is destructive and only provides local information. Furthermore, the sample preparation may induce some errors because the cutting and polishing could result in the tearing of poorly consolidated particles.

To address these limitations, Archimedes measurements are routinely performed in laboratories and industrial plants around the world [1,2]. As stated in [2], 'depending on experimental conditions, variations of up to + /- 20 % can occur for porosity rate values in the 1–5 % range', which can amount to uncertainties of 1 % range in absolute terms. Along a related characterization line, Helium pycnometry [2] allows to measure the true density of a fabricated part, with a potentially much better accuracy. However, Helium pycnometry is limited to samples of small volumes.

For the detailed analysis of part density, the technique of choice is X-Ray tomography or X-ray CT, since it usually allows, in addition to density estimation, to locate porosities or other process shortcomings within the tested volume [4–6]. This is clearly a major advantage over the other methods discussed [1,2]. However, X-Ray CT has certain

* Corresponding author.
*E-mail address:* florian.lebourdais@cea.fr (F. Le Bourdais).

https://doi.org/10.1016/j.addma.2022.103037
Received 24 March 2022; Received in revised form 11 July 2022; Accepted 11 July 2022
Available online 13 July 2022

limitations with respect to the part size and materials. Denser materials such as steels are often difficult to penetrate thus requiring high energy; moreover, there might also be some image artefacts. Besides, the image acquisition necessary for X-Ray tomography reconstruction is demanding in terms of both processing time and data storage. Despite these limitations, X-ray CT has become the most preferred method in industrial use cases for porosity detection.

In this respect, the objective of the present paper is to discuss the potential of an alternative technique, namely Resonant Ultrasound Spectroscopy (RUS, see e.g. [7,8]) to characterize AM materials. RUS is based on the excitation of elastic stationary waves in the part that can be analyzed in terms of resonance peaks. In addition to density measurements, RUS can provide useful insights on material properties. In this respect, a first interesting application of RUS is that, used in connection with numerical modelling techniques that solve the wave propagation equations, RUS has been used to accurately determine the elastic constants of a given material.

On a different line of investigation, the RUS technique is also suitable for defect determination, since the defects present in the part volume interact with the propagating waves and thus modify the resonance spectra. More precisely, the peaks can broaden, shift or even split [9]. For instance, the effect of cracks in Si wafers was fruitfully investigated using these properties using RUS in references [10,11]. Recently, the technique was also extended to investigate the properties cold-sprayed bonds and localize damage zones appearing during thermal loading [12]. It thus appeared interesting to test whether RUS could bring fruitful insights in the characterization of LPBF parts.

Relatedly, some authors in the RUS community have recently started exploring the applicability of RUS to samples manufactured by additive manufacturing. Trolinger et al. have investigated the potential of RUS to discriminate additively manufactured samples differing through small geometrical details with RUS [13]. A study on nickel samples performed by Rossin et al. investigated the ability to quantify the change in grain structure through heat treatment and hot isostatic pressing with RUS [14]. A study by McGuigan et al. explored the possibility of detecting defects in additively manufactured lattice structures using RUS [15]. Finally, another paper by Rossin et al. investigated the detailed texture effects that can be quantified through an homogenization approach of the polycrystal texture due to the LBPF process and compared it to destructive EBSD measurements [16].

As RUS data is known to be sensitive to a number of material imperfections, it was decided in the present work to focus on Lack of Fusion defects, which represent one very important type of defects in LPBF. To make sure that our observations were indeed only related to lack of fusion porosities, and not e.g. to cracks or keyhole porosities, our choice was to use a relatively friendly $AlSi_7Mg_{0.6}$ alloy for which optimized fabrication parameters are given by machine manufacturers. As a matter of fact, as opposed to structural aluminum grades often prone to hot cracking [17], $AlSi_7Mg_{0.6}$ can be printed without any major problems. Regarding methodology, our approach was first to manufacture a number of samples with widely varying process parameters, ranging from the optimal to severe lack of fusion domains, and to first characterize them with standard Archimedes and X-ray tomography techniques.

The next step was to look for correlations between RUS spectra characteristics and data coming from the other measurement methods. It should be noted that the measurand is consistent between techniques: in RUS, the excitation of volumic structural modes is not likely to be sensitive to surface roughness due to wavelengths that are much longer than the typical length of the roughness. Therefore RUS is expected to characterize closed porosity. As such the measurand is similar to that of the Archimedes technique, where the liquid is assumed to wet the open pores. This is also consistent with XCT, which is a choice technique for imaging the sample boundary, making the identification of closed pores possible.

The resonance spectra of the produced samples were thoroughly characterized in terms of peak quality factors, fundamental frequencies and Young's moduli, with the objective of identifying correlations with density or equivalently, porosity, defined as the volume fraction occupied by the pores. Our general objective is to investigate the potential of RUS to detect process deviations inside the parts generated by the L-PBF process.

## 2. Methods

### 2.1. Manufacturing of the samples used in this study

The material used in the present work is an $AlSi_7Mg_{0.6}$ alloy supplied as $N_2$ gas atomized powder by the Toyal company. The samples were manufactured with the L-PBF (Laser powder Bed Fusion) process and with only virgin powder, i.e. powder was not used for anything else between the delivery from the supplier and the manufacturing of the samples.

#### 2.1.1. Powder

The granulometry of the powder is quite high compared to the standard of the L-PBF process with values of the 10, 50 and 90 percentiles respectively of 27 μm, 40 μm and 59.5 μm according to the powder manufacturer data sheet.

A statistical analysis of the particle morphology was realized on about 80,000 powder particles projected on a screen and analyzed with image processing to determine the aspect ratio of the supplied powders, which provides information on the sphericity of the particles. A morphogranulometer (Morphologi G3S from Malvern Panalytical) was used to perform this analysis. For our Toyal $AlSi_7Mg_{0.6}$ powder, the aspect ratio is 0.78 (one means perfectly spherical). For a gas-atomized material, this powder has a rather low aspect ratio, but this did not cause any manufacturing issues.

The density of the powder was measured by helium gas pycnometry. After 100 measures, the mean value was equal to 2.67 $g/cm^3$ , with a standard deviation of 0.01 $g/cm^3$ , which is fully consistent with the theoretical bulk value of 2.68 $g/cm^3$ for this material as provided by the manufacturer data sheet. Even though the presence of entrapped bubbles from the gas atomization process cannot be excluded, it can nevertheless be assumed that the powder has a very low level of closed porosity.

#### 2.1.2. Experimental strategy

As mentioned in the introduction, the goal of this study is to test the ability of Resonant Ultrasound Spectroscopy to correlate with density data and possibly to detect process deviations inside the parts generated by the L-PBF process. To this end, two builds were realized under Argon (Ar) atmosphere in Farsoon FS271M machine, with a 275 × 275 $mm^2$ fabrication plate and a Gaussian shaped laser spot of circa 130 μm in diameter. The first build was made with a powder layer of 30 μm and the second build was made with a powder layer of 60 μm. The samples for each build are cylindrical with 10 mm in diameter and 15 mm height. Laser power ranged between 200 and 300 W in 25 W steps, and laser speeds were 500, 750, 1000, 1500 and 2000 mm/s. Hatches (that is, the distance between adjacent laser vectors) used were 0.17 and 0.21 mm. A rotation of 45° of the scan pattern was performed between powder layers. It should be mentioned that other strategies for rotation in between layers can be found in the literature, but this 45° rotation complies with the recommendations of the machine manufacturer for this type of materials. Also, in line with the machine manufacturer's recommendations, the last layer is submitted to a double laser scan, with the same parameters used for the fabrication of the previous layers. In all cases, the contour of the cylinders was realized with specific laser parameters, namely a power of 300 W and a scan speed of 700 mm/s.

As for their location on the build plate, four samples fabricated with an identical set of parameters were positioned on a same line perpendicular to the recoater motion, and without any supporting structure.

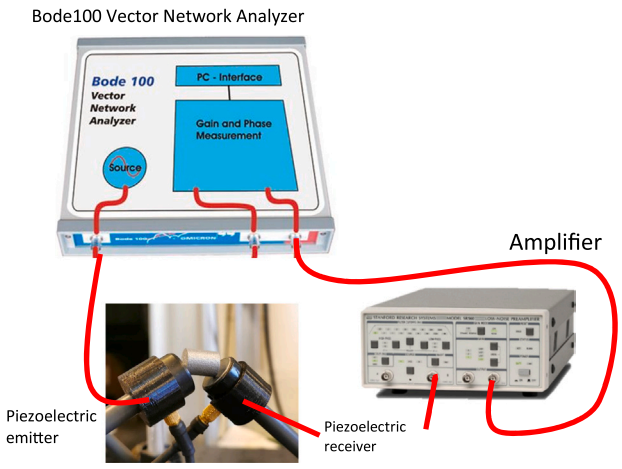


**Fig. 1.** Apparatus used in this study for making resonance measurements.

After fabrication, the samples were separated from the build plate using a band saw. It should be noted that neither post build heat treatments nor polishing procedures were performed on the samples prior to the characterizations. The density of each sample was measured by the Archimedes method and NDT techniques, applied as described in the next sections.

### 2.2. Archimedes density measurements

In the Archimedes density measurement, the relative density of an object is measured by the ratio between the apparent density and the real density of the material according to:

$$d = \frac{\rho_{apparent}}{\rho_{real}} \times 100 \quad (1)$$

where d is the relative density of the material ( %), $\rho_{\text{apparent}}$ is the apparent density of material (kg/m$^3$) and is measured on the part from the L-PBF process by the Archimedes' law, $\rho_{\text{real}}$ is the real density of the material (kg/m$^3$) that is defined by the theoretical density of the material, and is also measured on powder by Helium pycnometry.

The Archimedes' method consists in estimating the apparent density of material with three consecutive weight measurements:

- Of the dry sample (1)
- Of the sample submerged in a liquid (2)
- And finally, of the wet sample (3)

The apparent density is calculated with the formula:

$$\rho_{Apparent} = \frac{m_{Dry}}{m_{Wet} - m_{Submerged}} \rho_{Liquid} \quad (2)$$

Where $m_{Dry}$, $m_{Submerged}$ and $m_{Wet}$ are respectively the masses of the sample in Dry, Submerged and Wet form (kg), $\rho_{\text{Liquid}}$ is the density of the liquid used for the measurement (kg.m$^{-3}$).

The density of the liquid is controlled by the measurement of the weight of a reference quartz sample, the measurement being repeated approximately every 20 min. The liquid is installed below the balance, at least 1 h before starting the measures for the establishment of thermal equilibrium with the ambient atmosphere. To ensure that the liquid gets into the open pores, the samples are placed in a vacuum chamber during 10 min before submerging in anhydrous ethanol, then placed under vacuum between 10 and 20 min. The vacuum is realized with a primary vane pump. Whereas the measurements of the dry and submerged masses is relatively straightforward, special care is required for the measurement of the mass of the wet sample to ensure that the liquid is still within the pores. To do so, the sample is quickly removed from the fluid, enveloped in an absorbing media and weighted before the ethanol evaporates.

### 2.3. Ultrasonic resonance measurements

#### 2.3.1. Spectrum measurements

In this study, ultrasonic resonance measurements were performed with the apparatus shown in the diagram in Fig. 1.

The apparatus consisted of a Bode 100 Vector Network Analyzer (OMICRON electronics Gmbh), a SR560 Low Noise Voltage Preamplifier (Stanford Research Systems) and two piezoelectric shear wave transducers for contact measurements V153-RM (Olympus). One piezoelectric transducer was connected to the source output of the network analyzer while the other one was connected to its input. The measurement mode was set to transmission.

Cylindrical samples were positioned so as to be able to resonate freely without blocking parts of their surface. This was done by carefully hinging their top and bottom faces on the surface of the piezoelectric transducers (see Fig. 1).

Measurements were made over a frequency range 95–495 kHz, with 40,000 measurement points and a receiver bandwidth frequency setting corresponding to 100 Hz. They were carried out at least twice for each sample, comparing successive measurements and checking that the first 5–10 peaks were detected at identical positions. As a matter of fact, RUS measurements are repeatable, but sensitive to the way the transducers and specimen are positioned, see [7,8,18] that discuss this issue. This yielded data that consists of 40000 points and two values at each point

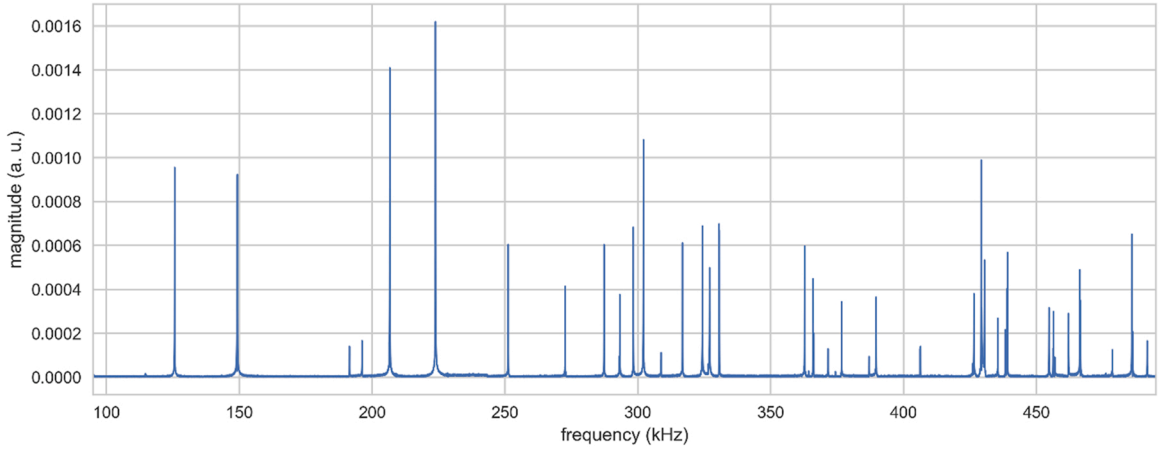


**Fig. 2.** Sample measurement showing obtained magnitude data as a function of frequency. The sharp peaks appearing are the resonance frequencies of the sample.

(magnitude and phase). Subsequently, only the magnitude component was used for processing (which is standard procedure in the RUS technique) Fig. 2.

The acquired data was processed in three distinct ways: quality factor extraction, fundamental resonance frequency extraction and Young modulus computation under an isotropy hypothesis.

#### 2.3.2. Fundamental frequency and quality factor extraction

For each spectrum, a peak extraction procedure was applied. The peak extraction procedure was parametrized by a minimal peak amplitude, a minimal prominence parameter (how much a peak stands out from the surrounding baseline of the signal, defined as the vertical distance between the peak and its lowest contour line), a minimal distance between peaks and a minimal peak width value. These settings were manually selected for each analyzed spectrum to minimize the number of falsely identified peaks.

Once peaks were identified, a Lorentzian function was fitted on the magnitude data around the peaks using LMFIT [19]. The functional form of the Lorentzian function used is

$$X(f, A, \quad \mu, \quad \sigma) = \frac{A}{\pi}\left(\frac{\sigma}{(f-\mu)^2+\sigma^2}\right) \tag{3}$$

where $A$ is the amplitude, $f$ the frequency, $\mu$ the center frequency and $\sigma$ the characteristic width of the peak. The fit is carried out on the three parameters $A, \mu, \sigma$. Once the fit has been computed, the full-width at half maximum (equal to $2\sigma$ under this model), is transformed into a non-dimensional quality factor by the formula $Q = \frac{\mu}{2\sigma}$. The typical uncertainty (due to reproducibility, gridding, fit procedure effects) for a fit on a given peak of reference single crystal samples is around 15 Hz on the frequency position, while that associated with quality factors is 900 (no unit).

For each spectrum, the outcome of this procedure is then a set of peak frequencies and their associated quality factors. We call fundamental resonance frequency the frequency of the first peak that was identified.

#### 2.3.3. Young modulus computation under an isotropy hypothesis and reduced number of frequencies

The spectrum of a given sample can be used to identify the elastic stiffness coefficients of the material under test considered elastically homogeneous via an inverse procedure called RUS (see e.g. [7,8,18]). Briefly, assuming the geometry and the density to be known, it consists in identifying the independent parameters of the symmetric $6 \times 6$ $C_{ij}$ Voigt matrix that minimize the objective function

$$F = \quad \sum_{k=1}^{K}\left(\frac{f_k^{exp} - f_k^{mod}(C_{ij})}{f_k^{exp}}\right)^2 \tag{4}$$

In Eq. 4, $f_k^{exp}$ are the measured resonance frequencies, while $f_k^{mod}$ are the modelled resonance frequencies.

In our setting, we decided to use the inversion process under the following assumptions:

- isotropy of the samples, i.e. the stiffness can be described by two independent coefficients, $c_{11}$ and $c_{44}$
- use of only the K= 2 lowest frequencies to minimize the objective function $F$

To go into more details, we parametrized the material by the elastic constants $c_{11}$ and $c_{44}$. The Voigt matrix then reads

**Table 1**
Estimates for partial derivatives of the first two resonance frequencies with respect to elastic constants used in this study.

| Resonance frequency number | $\frac{\partial f}{\partial c_{11}}$ (kHz/GPa) | $\frac{\partial f}{\partial c_{44}}$ (kHz/GPa) | $\delta$ ( %) |
|---|---|---|---|
| 1 | 0.00 | 2.25 | 0.00 |
| 2 | 0.24 | 1.92 | 11.30 |

$$C_{ij} = \begin{bmatrix} c_{11} & c_{12} & c_{12} & 0 & 0 & 0 \\ c_{12} & c_{11} & c_{12} & 0 & 0 & 0 \\ c_{12} & c_{12} & c_{11} & 0 & 0 & 0 \\ 0 & 0 & 0 & c_{44} & 0 & 0 \\ 0 & 0 & 0 & 0 & c_{44} & 0 \\ 0 & 0 & 0 & 0 & 0 & c_{44} \end{bmatrix}$$

with $c_{12} = c_{11} - 2c_{44}$. The Voigt matrix is used while assembling mass and stiffness matrices M and K with the Rayleigh-Ritz method. The matrices allow solving the classical vibration eigenvalue problem $(2\pi f)^2 M_{ij} a_j = K_{ij} a_j$ where $a$ is the eigenvector associated to eigenfrequency $f$ (the solutions of this equation, sorted in ascending order, are denoted by $f_k^{mod}$ in Eq. 4), see e.g. [7,8].

The objective function is minimized using a conjugate gradient (CG) solver found in the SciPy software package [20]. An explicit gradient computation was provided based on a standard formula for the Rayleigh-Ritz method (see e.g. [7,18]). The CG algorithm iteratively modified the values of the $c_{11}$ and $c_{44}$ parameters until the value of the cost function gradient was less than $10^{-6}$. The resulting optimization yielded RMSE errors less than 0.2 % for all samples.

Finally, the elastic constants $c_{11}$ and $c_{44}$ were converted to a Young modulus value according to the formula $E = \frac{c_{44}}{c_{11}-c_{44}}(3c_{11} - 4c_{44})$.

Two remarks can be added at this stage, and will be further addressed in the discussion section below.

The first is that one does not know a priori if the inversion procedure will converge to the correct solution. In particular, if the function $F$ is not sensitive to one of the elastic parameters (i.e. if its partial derivative $\frac{\partial F}{\partial p} \approx 0$), it should not be possible to determine this parameter. Since $F$ is in turn dependent on the modelled resonance frequencies, other authors have shown that a crucial question is how much the used frequencies depend on the elastic constants used. Many authors have found that the first resonance frequency only depends on the shear elastic constant $c_{44}$ (e.g. [8,18,21]). We have come to the same conclusion. In addition, we found that in our cylindrical isotropic case, the second resonance frequency is quite sensitive to the second elastic constant, $c_{11}$, allowing the inversion to succeed with only two recorded frequencies. This is different from Nejezchlebová et al. [21] who showed that with rectangular geometries the first few resonance frequencies were insensitive to the second elastic coefficient used. Our numerical estimates of $\frac{\partial f}{\partial c_{11}}$, $\frac{\partial f}{\partial c_{44}}$ and $\delta = \frac{\frac{\partial f}{\partial c_{11}}}{\frac{\partial f}{\partial c_{11}} + \frac{\partial f}{\partial c_{44}}}$ are shown in Table 1.

The second remark concerns the dependency of the elastic constants and of the Young modulus with respect to the density of the sample. It is well known that porosity usually reduces the velocity of the medium and hence also reduces the elastic constants and the Young modulus [22,23]. Therefore, measuring the Young modulus using RUS should, in theory, be sensitive to the porosity volume fraction.

### 2.4. X-ray tomography

Without going into unnecessary details (see e.g. [24] for a discussion of the basic principles), X-ray Computed Tomography (XCT) is a multi-step procedure starting with an acquisition of the projections, which undergo a reconstruction procedure followed by the measurements and/or defect detection. During the scanning procedure, the part is placed between an X-ray source and a 2D detector and several

**Table 2**
The optimized XCT scanning parameters for the cylinder.

| Parameter | Value |
|---|---|
| Voltage, kV | 112 |
| Current, μA | 115 |
| Exposure, s | 1 |
| Filter/Cu, mm | 0.6 |
| Projection,- | 900 |
| SOD/SDD, mm | 40; 45 / 500 |
| Voxel size, μm | 16; 18 |

hundreds of projections are recorded while the part is rotated. The quality of the CT result depends on the selection of the scanning parameters (current, voltage, exposure time, etc.), which need to be optimized considering the size, geometry, and the material of the part [25,26].

The tomographic acquisitions have been carried out using a Viscom XT9225D micro-focus open X-ray tube, with a maximum voltage of 225 kV and a maximum power of 320 W. The detector is a matrix of photodiodes with CsI scintillator, brand Perkin Elmer, model XRD 0822, having 1024 × 1024 pixels of 200 μm. The cylinder to be analyzed is placed between the source and the detector on the rotary stage and the projections are acquired for complete 360° rotation. The Source-to-object distance (SOD) is selected considering the field of view of the X-ray cone. The parameters used for XCT are summarized in Table 2.

A voxel-based volume is obtained from the reconstruction of the projections with a dedicated filtered-back projection algorithm. VGStudio Max 3.5 is used for the reconstruction and post-processing of the volumetric dataset. The in-built VGDefX porosity detection algorithm was utilized for porosity quantification with default settings (Material definition: "Use determined threshold"; Probability threshold: 1; Min size: 8 voxels). Fig. 3 is a pictorial representation of the data processing step. The smallest pore size that can be reasonably detected is around three voxels.

## 3. Results

### 3.1. Analysis of Archimedes density as a function of VED

Before turning to the thorough characterizations that are the main objective of the present work, our purpose in this subsection is to present the Archimedes data obtained for all samples fabricated in this design of experiment. To do so, results will be shown as a function of the energy input used for the fabrication of each sample. Unfortunately, the definition of this energy of a given sample is not an easy task, see e.g. reference [27] for a detailed discussion on this issue. Whereas the uses of laser power and scan velocity are straightforward, the energy density

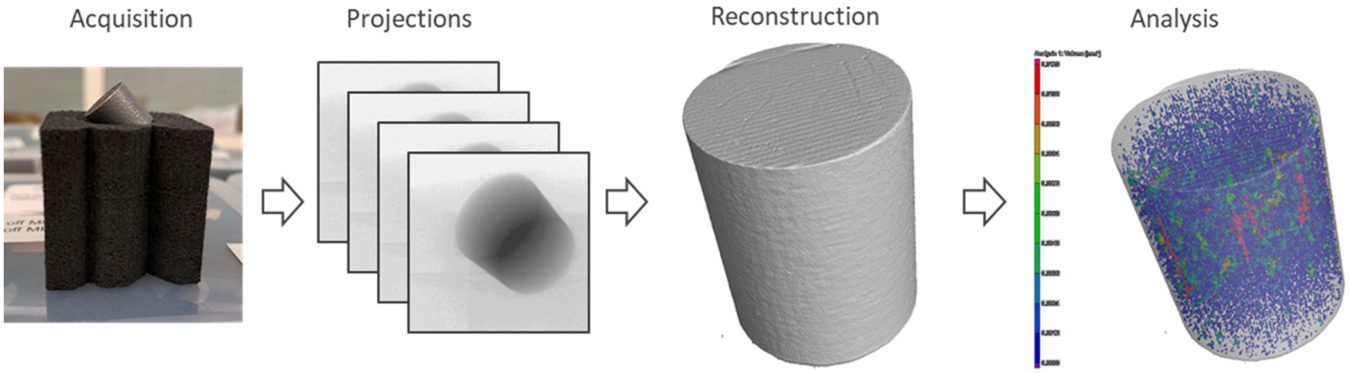


**Fig. 3.** The various steps of XCT based defect analysis of the AM cylinders.

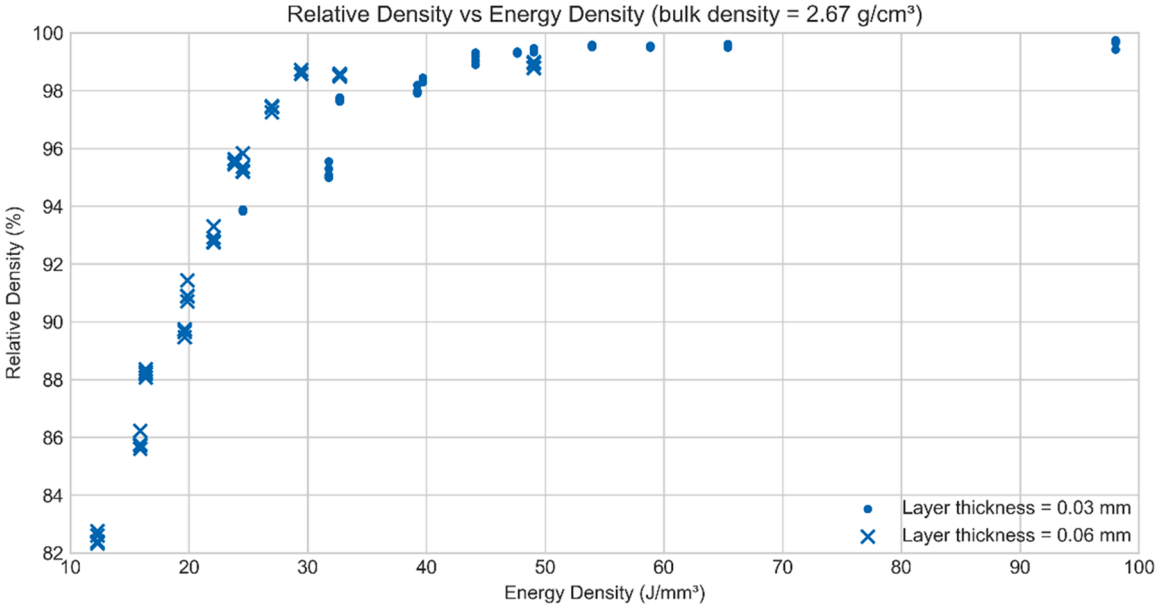


**Fig. 4.** Relative density vs. Energy density on 96 samples build with various powders and parameters.

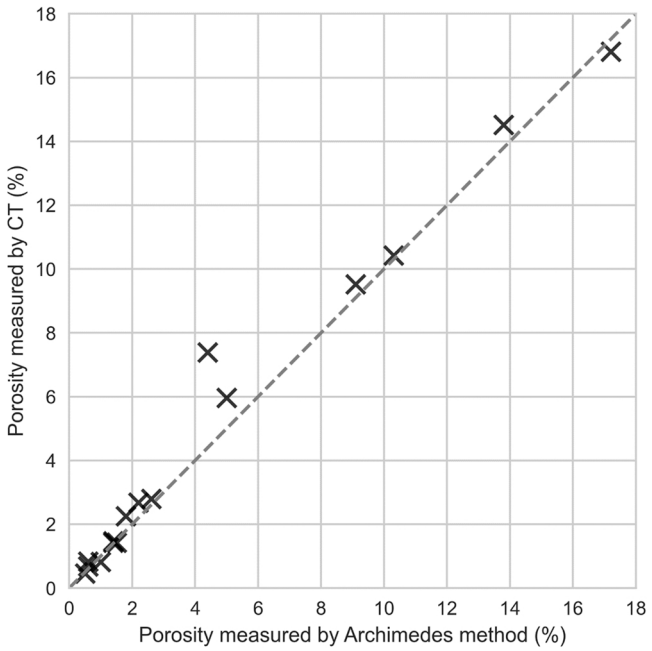


**Fig. 5.** Porosity values obtained from XCT and Archimedes method for the samples under investigation.

can either feature the laser spot area (Volumetric Energy Density, VED) or the layer thickness and hatch spacing (Energy per Built Volume, EBV). The VED is probably better to understand the local physics of the process, but from an engineering standpoint the EBV allows to account for heat accumulation between passes and layers [27].

In addition, it can be argued that what really matters is the actual energy input, therefore an absorption coefficient, taking into account the amount of energy lost to the surroundings, should preferably be used. However, the measurement of this absorption coefficient is not an easy task, so with all these limitations in mind, the results will be presented for purposes of comparison according to the energy density defined in Eq. (5) as follows:

$$EBV = \frac{P}{V\,H\,e} \tag{5}$$

In this formula, EBV is expressed in J/mm$^3$ , P is the Laser Power (W), V is the Laser Speed (mm/s), e is the Layer thickness (mm) and H is the Hatch (mm).

#### 3.1.1. Results on 2 building jobs

The relative density measurement was performed on the 96 samples built in the 2 jobs. Parameters of each sample used in the energy density calculation vary between values in brackets: Power [200; 300], Speed [500; 2000]; Hatch [0.17; 0.21] and Layer thickness [0.03; 0.06] to obtain a wide measuring range. The results are shown in Fig. 4. EBV is seen to vary between values of 12.25 and 98 J/mm$^3$ and the relative density increases steadily with EBV until 30–40 J/mm$^3$, then reaches a "stable" zone from 40 J/mm$^3$ on with over 98 % of relative density. The data do not exhibit the decrease often observed at high EBV and attributed to keyhole porosities. As a matter of fact, it should be mentioned that no large spherical voids were identified by XCT, indicating that we did not venture into too large energy densities. Within each set of data, a certain dispersion can be observed, but the trends are nevertheless quite consistent, supporting the validity of the energy density scaling proposed in Eq. (5).

Out of the total of 96 manufactured samples, 16 specimens (eight from the build with a powder layer of 30 μm and the other eight from build made with a powder layer of 60 μm) were selected for detailed study with XCT and RUS. The goal was to have a wide range of density variations among the samples to induce variability factor in the analyses. The results are presented and discussed in the following sections.

### 3.2. Validation of Archimedes and analysis of energy as a function of density

#### 3.2.1. Correlation between Archimedes and CT measurements

It is desirable to have a reliable technique that is fast, economical and accurate; the Archimedes is one such method to have a first-hand density/porosity measurement on a large scale. However, it is always safe to have a validation with more sophisticated technique such as X-ray CT. The plot in Fig. 5 presents the comparison of density (or equivalently in this article, porosity) measurements between CT and Archimedes.

As a global observation of the plot in Fig. 5, there is very good agreement between the results for 15 out of 16 measurements, which is also consistent with similar studies from the literature [1,6]. Also, since the relationship looks like a linear one, we use the Pearson correlation coefficient to quantify it. We obtain a value of 0.989, which strongly

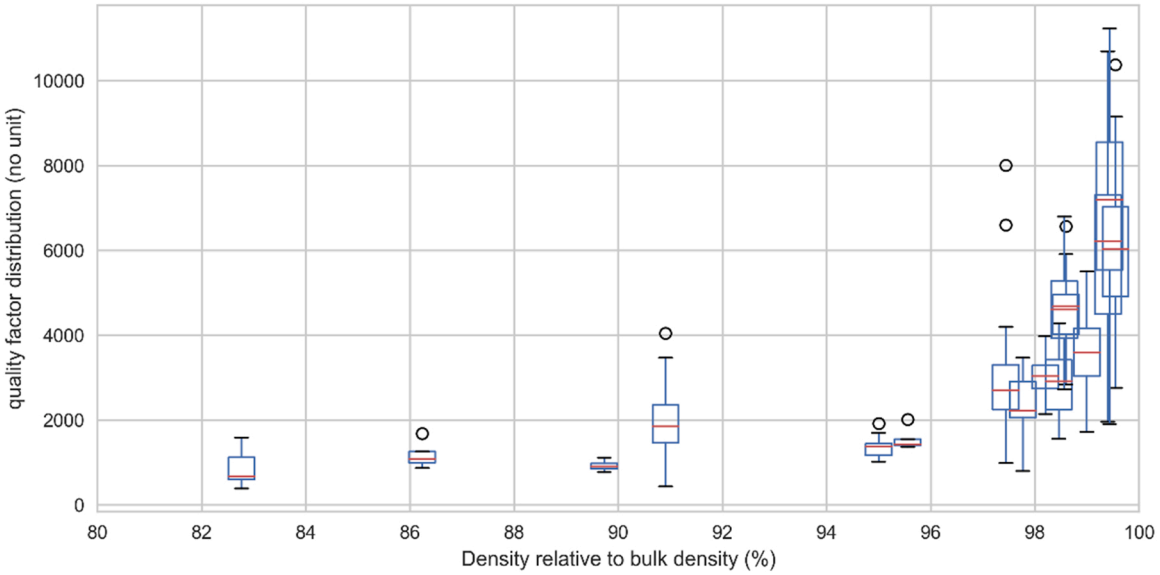


**Fig. 6.** Boxplot of the quality factors for all samples in this study.

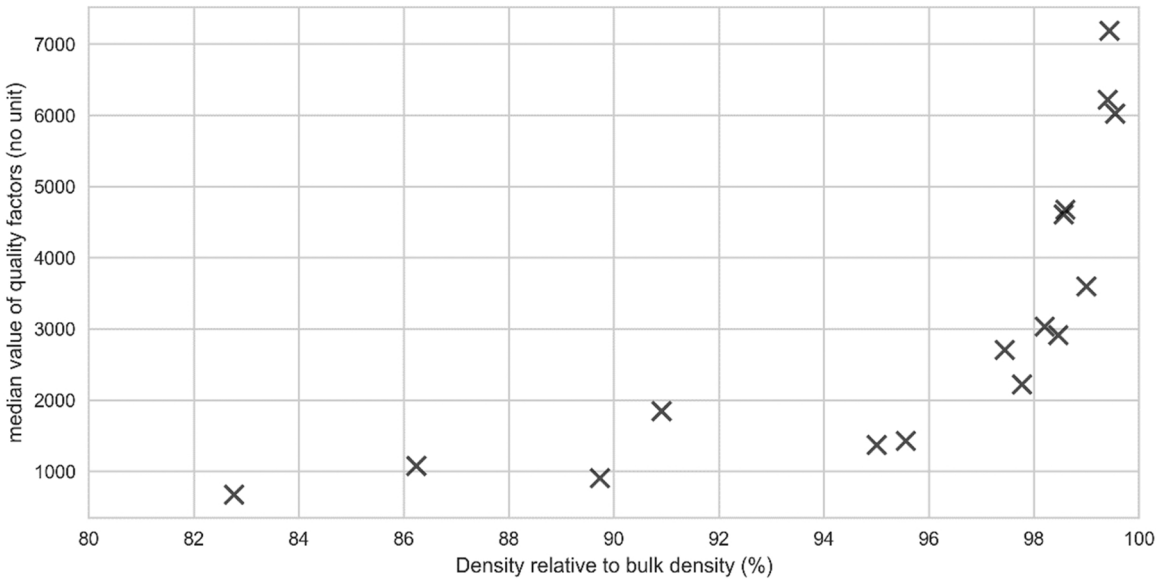


**Fig. 7.** Scatter plot of the median value of the quality factors for all samples in this study.

suggests that the two density measures are in linear relationship to each other. However, there are two points that exhibit overestimation in CT porosity measurements; it can be noted that these two points belong to a somewhat medium range of porosity values and the amount of lack of fusion pores is a bit critical in this range as it can go undetected with the resolution we used. Preliminary results using high-resolution synchrotron rays, that are outside of the scope of the present work, indeed seem to indicate that individual powder grains can be observed in lack of fusion porosities. Nevertheless, in the following we consider that these results obtained using X-ray tomography validate the Archimedes density measurement, which will be used from now on as the reference density measurement for comparison with the RUS data.

### 3.3. Resonance measurements

#### 3.3.1. Quality factors

Since the extracted quality factors consist, for each sample, of several values, their distribution is characterized by its quartiles Q1, Q2 and Q3, the median value being given by Q2 and shown as a boxplot in Fig. 6:

In Fig. 6, the box is drawn from Q1 to Q3 with a line at the median, Q2. The whiskers extend from the edges of box to show the range of the data. The position of the whiskers is set to 1.5 * IQR (the interquartile range IQR is equal to Q3 - Q1) from the edges of the box, which is a standard choice for this parameter. In such a context, points past the edges of the whiskers should be considered as outliers. In some instances the IQR remains very small (say less than 500) but overall the IQR is

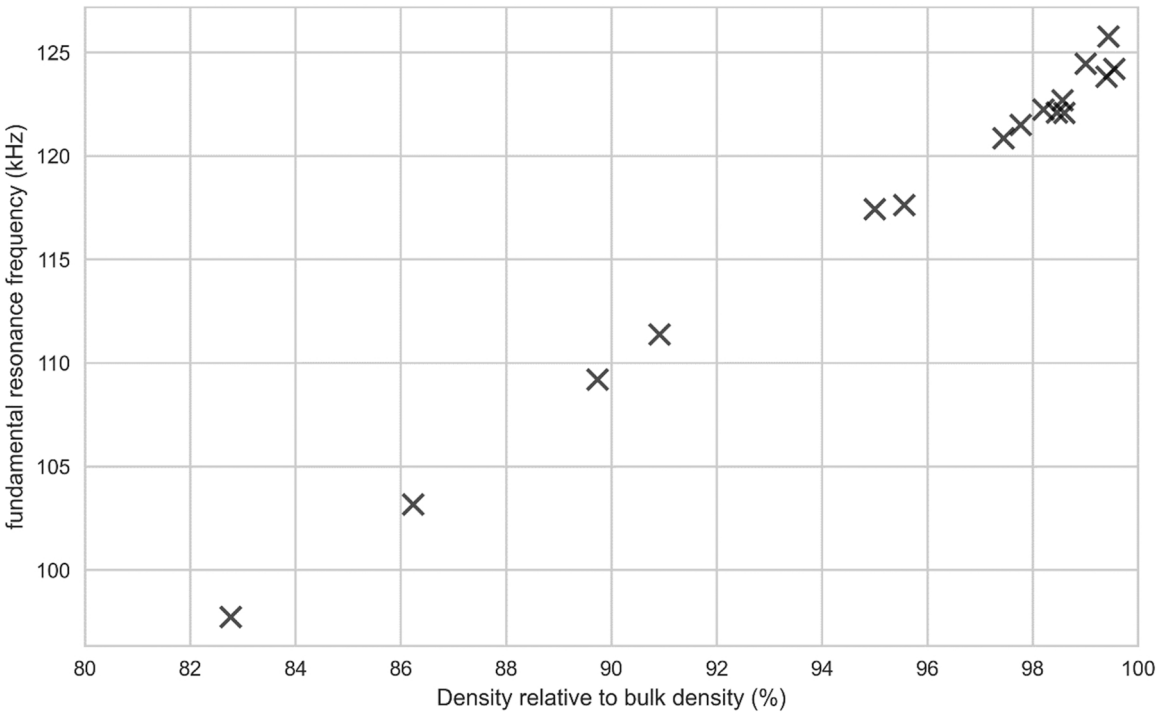


**Fig. 8.** Scatter plot of the fundamental resonance frequency for all samples in this study as a function of density relative to bulk density.

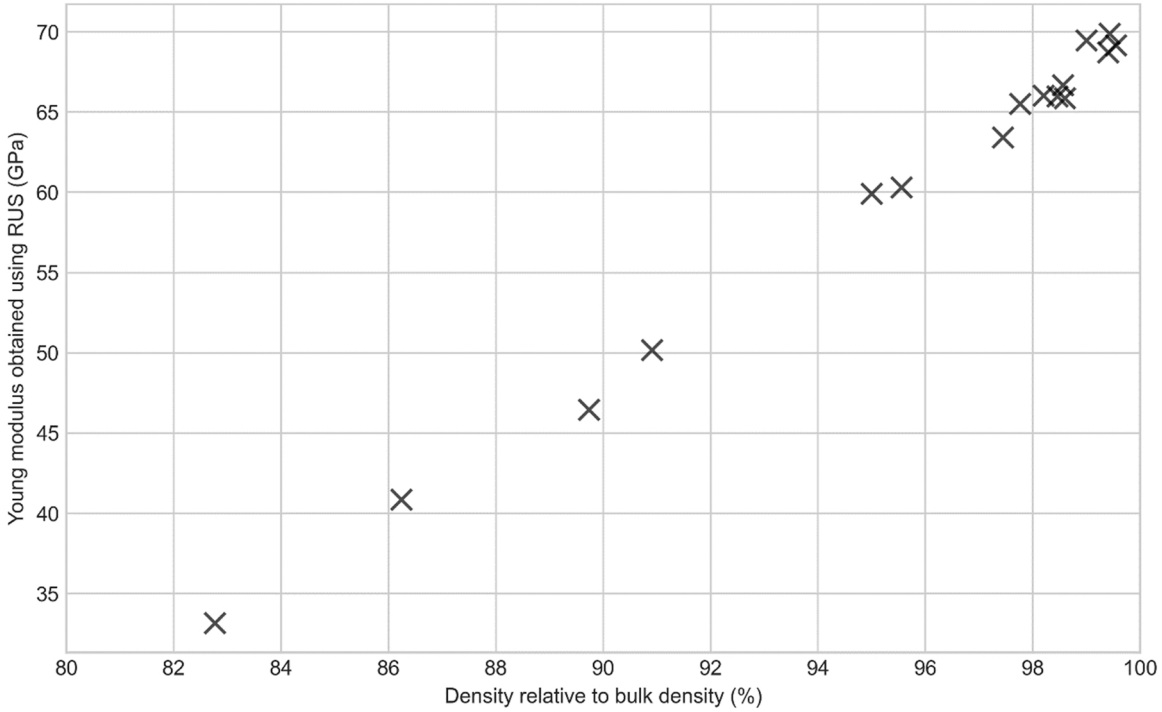


**Fig. 9.** Young modulus for samples in this study as a function of density relative to bulk density.

often above 1000 which is consistent with the uncertainty on the quality factors of a given peak, estimated at 900 in the methods section.

If we summarize the distribution by its median value, we present the plot in Fig. 7.

As the plot in Fig. 7 shows, the quality factors seem, on average, to be higher the denser the part is. This correlation seems to hold over the full range of densities investigated in this study (approximately 80–100 %). Although there is some variance in the relationship, it seems this indicator can easily be used to quantify the quality of the obtained part. Since the relationship is strongly nonlinear, we used the Spearman correlation coefficient to quantify it. The computed value for the Spearman $\rho$ was equal to 0.964, indicating a strong relationship between the density and the median value of the quality factors. The quality factor data appears to be very sensitive to low level of porosities, an interesting feature for the characterization of AM materials.

#### 3.3.2. Fundamental frequency

The fundamental frequency is plotted relative to the sample density in Fig. 8:

Fig. 8 shows a nearly linear correlation between the fundamental resonance frequency and the density measurements. On the one hand, the sensitivity to density is lower compared to the median quality factors, but, on the other hand, the spread of the data is much lower. The fundamental resonance could then be used to quickly quality check samples after they have been built. Since the relationship looks linear, we used Pearson's linear correlation coefficient to quantify it. Pearson's $\rho$ was equal to 0.997 for this data, indicating a strong monotonous relationship between density and fundamental frequency.

#### 3.3.3. Young modulus computation under an isotropy hypothesis and reduced frequency number

The Young modulus obtained under the isotropy hypothesis is plotted relative to the sample density in Fig. 9:

As with the fundamental frequency plot, the relationship between the Young modulus and the relative density seems to be linear. It should be noted that the values obtained for our best samples (circa 71 GPa are typical of good quality L-PBF fabricated Aluminum foundry alloys [28]).

Since the relationship looks like a linear one, we use the Pearson correlation coefficient to quantify it. We obtain a value of 0.952, which indicates a strong relationship between density and Young modulus.

## 4. Discussion

In this section, we discuss the results shown in the previous sections. We first discuss the correlation concerning the first resonant frequency and then the one concerning the Young modulus.

### 4.1. Explanation of the first resonant frequency correlation

In a very general manner, the individual resonance frequencies of a sample can be written in the form shown in Eq. (6) [16].

$$f_r = \frac{n}{2L}\sqrt{\frac{C^*}{\rho}}, \tag{6}$$

where $n$ is the mode number, $2L$ is the wave propagation distance, $\rho$ the density and $C^*$ the effective elastic constants along a given direction. As can be seen in this expression, the effective elastic constants and density have an opposite effect on resonance frequencies. One question is then, which of these two effects is larger in the samples found in our study?

The first part of the answer to this question is given by the analysis of the sensivity of $f_0$, the fundamental frequency to $c_{11}$ and $c_{44}$. Since we computed the partial derivatives of the fundamental frequency numerically in Table 1, we know that $f_0$ does not depend on $c_{11}$. Hence we can conclude, as Nejezchlebová et al. [21] that $f_0 = \alpha\sqrt{\frac{c_{44}}{\rho}}$, with $\alpha$ a constant.

The second part of the dependency is then in the relation between the Young modulus $E$ and the two elastic constants $c_{11}$ and $c_{44}$. Computing the quantity $\delta_E = \frac{\frac{\partial E}{\partial c_{11}}}{\frac{\partial E}{\partial c_{44}}}$, we obtain that

$$\delta_E = \frac{c_{44}^2}{(c_{11}-2c_{44})(3c_{11}-4c_{44})}. \tag{7}$$

Numerically, we obtain a value of $\delta_E$ close to 7 %. Neglecting the effect of $c_{11}$, we can then conclude that the relationship between $c_{44}$ and

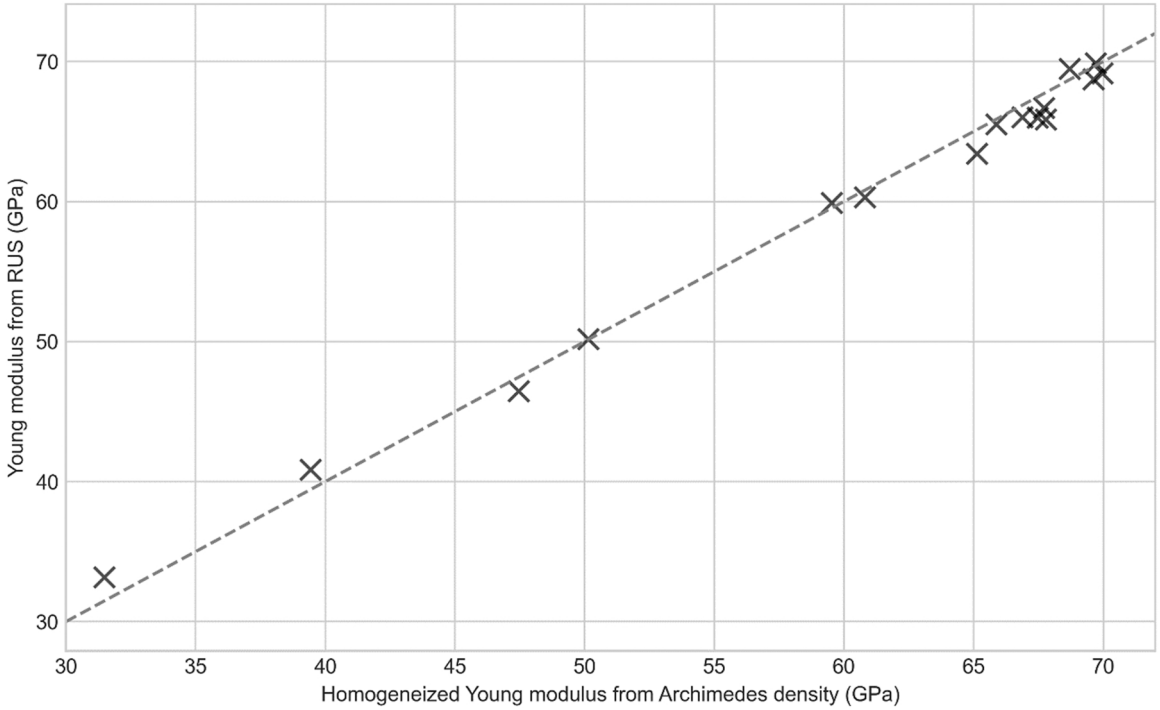


**Fig. 10.** Young modulus obtained from RUS versus Young modulus obtained from homogeneization theory and Archimedes measurement.

$E$ is approximately linear, leading to a relationship with the fundamental frequency as $f_0 = \beta\sqrt{\frac{E}{\rho}}$, where $\beta$ is a constant.

We can now compute the relative change of $E$ and compare it to the one in $\rho$ to explain the relationship found in Fig. 9. The density of the samples in our study varied between 83 % and 100 % relative density, thus a 1.2 ratio, which would tend to increase the first resonant frequency. On the other hand, the Young modulus varied between 31 and 71 GPa, hence a 2.3 ratio, which would tend to decrease the first resonant frequency. Overall, the effect should thus be a decrease, as the contribution from the Young modulus is stronger compared to that of the density. Further evidence of this is seen in the correlation between the first resonance frequency and density that has been reported in the results, where the fundamental frequency increases with density. These observations lead to a further question: can the effect of porosity on the Young modulus be predicted with a "simple" homogenization theory model?

### 4.2. Homogenization theory and the effective Young modulus

Assuming a mechanical model of a linear elastic medium made of a matrix with aluminum or $AlSi_7Mg_{0.6}$ bulk properties and containing stress free cavities that have a volume fraction of macro porosity p, we can use Eshelby's method to propose effective properties at the macro scale, following [29]. To apply the dilute method, we need to specify a bulk Young modulus and bulk Poisson coefficient. Doing so leads us to the expression for the effective Young modulus in Eq. (8):

$$E = E_0(1 - 10{\cdot}\nu{\cdot}p) \tag{8}$$

where $E_0$ and $\nu$ are respectively the bulk Young modulus and the Poisson coefficient of the defect-free material and $p$ is the macro porosity. Applying this formula to the Archimedes density measurements, we obtain a Young modulus that can be compared to the one determined by the RUS method and reported in Section 3.3.3. In Fig. 10, we use a value of 71 GPa for $E_0$, as found by our own RUS measurements for practically 100 % dense samples. In the absence of specific data for the Poisson coefficient, we took from the literature a typical value of 0.32 for $\nu$ [30]. It should be noted that the results are relatively insensitive to reasonable variations of $\nu$ around 0.32. In any case, Figure 13 displays the Young modulus measured by RUS and the one deduced from the Archimedes density measurement with Eq. (8).

As Fig. 10 shows, an excellent correlation is observed over the full range of densities in our study. This finding supports the capacity of RUS to accurately measure Young's moduli in fully dense and porosity-prone materials.

Nevertheless the agreement can be considered a priori surprising due to the drastically simplified RUS inverse model fitting process compared to what is usually carried out in the literature ([7,8,18]), since we only used the first two resonance frequencies measured and modelled the elastic behavior with a linear isotropic model. This way of obtaining the Young modulus can be criticized since we do not make sure that the fitted model is robust and fits higher order resonance frequencies, which could result in misleading conclusions. Furthermore, we model the sample as isotropic and homogeneous, which is, strictly seen, not true since the obtained samples are polycrystals that are textured due to the thermal heat flux that is dominantly oriented along the vertical direction (see [14,16,31] for discussion of this phenomenon). A counter argument to this objection comes from studies on effective properties and homogenization. If we take the obtained RUS elastic constants as representative of the effective texture of the aggregate structure, it is not necessarily surprising that an isotropic constitutive elastic law describes the investigated samples well. Indeed, Latypov et al. investigated the use of polycrystal homogenization schemes and showed that the effective homogeneous medium does not necessarily feature the same anisotropy that is characteristic of the single grains [32]. An overall better approach to the RUS characterization problem would have been to investigate different elastic symmetries and select the model that best describes the first 50 resonance frequencies, such as Evans et al. [33] have done recently. However, this is a hard to automate and time-intensive process that would not have allowed investigating a large number of samples in the way we have done here. Most papers published in the RUS community investigate only two or three samples instead of tens, due to the fact that the most difficult part of RUS inversion is to robustly solve the pairing problem between computed and measured frequencies, some of

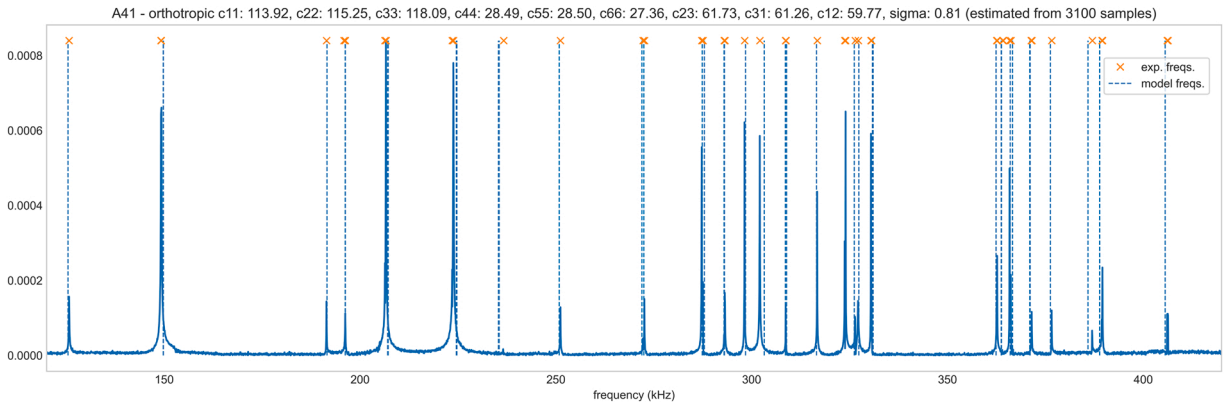


**Fig. 11.** Elastic characterisation of an almost dense sample from our study using orthotropic elastic behaviour (nine coefficients). The modelled peaks are overlaid as dashed lines on top of the experimentally measured spectrum.

**Table 3**
Elastic constants obtained with orthotropic bayesian RUS inversion. Mean values and standard deviations obtained from samples are compared to values obtained from an isotropic approximation (Young modulus 75 GPa, Poisson coefficient 0.34).

| Coefficient | C11 | C22 | C33 | C44 | C55 | C66 | C23 | C13 | C12 |
|---|---|---|---|---|---|---|---|---|---|
| Mean value (GPa) | 114.1 | 115.1 | 118.1 | 28.5 | 28.5 | 27.4 | 61.8 | 61.3 | 59.9 |
| Standard deviation (GPa) | 2.2 | 2.1 | 2.2 | 0.2 | 0.2 | 0.1 | 2.0 | 2.1 | 1.6 |
| Closest isotropic approximation (GPa) | 115.8 | 115.8 | 115.8 | 28.1 | 28.1 | 28.1 | 59.5 | 59.5 | 59.5 |

which could have gone undetected (e.g. due to weak coupling to the transducers) [34]. Some authors claim that in order to rigorously solve the inverse problem, mode shapes also need to be measured and matched to simulated vibration modes [35,36] while at least one author showed that it was possible to solve the problem correctly without these additional measurements [37]. We have performed a thorough characterization of a single sample and found that we could fit its first 44 frequencies using Bayesian inversion, in the way discussed in [38] and assuming that no frequency was left undetected. Our result is shown in Fig. 11, where the modelled resonant frequencies are overlaid on top of the experimental spectrum. We chose an orthotropic elastic model to describe the sample, following recent results in homogenization theory described in [16]. The obtained elastic constants are in Table 3. As can be noted, even though the material is not isotropic, the obtained elastic constants point to a relatively mild anisotropy, which tends to justify the isotropy hypothesis used in this work. Our conclusion is further supported by a recent study that also found elastically isotropic behavior for a AlSi10Mg in the L-PBF as printed state using RUS [39].

## 5. Conclusions

Our main purpose in this work was to demonstrate the potential of the RUS technique for the characterization of the density in LPBF materials. To this end, we have focused on the use of three non-destructive methods: Archimedes procedure, X-ray tomography and resonant ultrasound spectroscopy. We fabricated $AlSi_7Mg_{0.6}$ samples with significantly different process parameters, resulting in varying amounts of porosity. A first result is that we demonstrated that all three techniques were sensitive to the varying levels of porosity, with a very good correlation between Archimedes and XCT data. A major conclusion of our work is that RUS is a very interesting candidate for studies in additive manufacturing, since it provides qualitative (quality factors) and quantitative (resonance frequencies, Young modulus) data that compare favorably with the density data from other techniques.

More precisely, the quality factors and their median can be used as relative comparisons to reference samples. The same can be said of the fundamental resonance frequency. In our experience, these measurements can be done in a short amount of time and do not necessitate much expertise for implementation. Although these properties certainly vary with the geometry of the sample (we used only cylinders in our study, so we did not experience this effect), we believe that they can be useful when assessing repeatability or variability of small series of specimens, including those of large dimensions and with complex geometries. Another valuable point is the ability to obtain quantitative estimates of elastic parameters, the Young modulus in this study. This information can be compared to macroscopic measurements like tensile tests or to literature values, for example to guide the user in the understanding of varying machine parameters.

Further work in this direction of research includes taking into account defects such as keyhole porosity. A step further from density measurements, preliminary results show that RUS data can be sensitive to networks of cracks that cannot be detected by the simpler Archimedes method and with an ease-of-use that is superior to X-ray tomography. This could be investigated using, for instance, other aluminum alloys prone to hot cracking. Another line of research could be to implement fully automated RUS inversion with a large number of resonant frequencies. Existing papers in the literature have tackled this problem for attenuative biological media [37], but these works have not been further pursued in the domain of highly resonating metallic materials since.

## CRediT authorship contribution statement

**Garandet Jean-Paul:** Writing – review & editing, Writing – original draft, Validation, Methodology, Conceptualization. **Bergeaud Vincent:** Writing – review & editing, Supervision, Conceptualization. **Bonnefoy Vincent:** Project administration, Conceptualization. **Ly Camille:** Writing – review & editing, Software, Investigation, Data curation. **Rathore Jitendra Singh:** Writing – review & editing, Writing – original draft, Methodology, Investigation, Data curation. **Vienne Caroline:** Methodology, Conceptualization. **Pellat Michel:** Writing – review & editing, Writing – original draft, Methodology, Investigation. **Le Bourdais Florian:** Writing – review & editing, Writing – original draft, Software, Methodology, Investigation, Data curation, Conceptualization.

## Declaration of Competing Interest

The authors declare that they have no known competing financial interests or personal relationships that could have appeared to influence the work reported in this paper.

## Data Availability

The data that has been used is confidential.

## Acknowledgments

The authors gratefully acknowledge their indebtedness to Jérôme Laurent (CEA) for his helpful support and comments regarding the implementation of the RUS measurement technique. Our gratitude also extends to Samuel 'Der Fuchs' Le Goupil for his unflinching energy in driving the Inflexion Positive project.

The authors also thank the five anonymous reviewers, who substantially contributed to the clarity of this article.

## Appendix

CT and Archimedes Data.

| Sample name | Porosity measured by CT ( %) | Porositiy measured by Archimedes method ( %) |
|---|---|---|
| A8 | 0.46 | 0.5 |
| A44 | 0.68 | 0.6 |
| A28 | 0.83 | 0.6 |
| A20 | 1.43 | 1.5 |
| A40 | 2.25 | 1.8 |
| A32 | 2.68 | 2.2 |
| A1 | 5.96 | 5.0 |
| A4 | 7.39 | 4.4 |
| B8 | 0.82 | 1.0 |
| B13 | 1.42 | 1.4 |
| B42 | 1.47 | 1.4 |
| B34 | 2.80 | 2.6 |
| B30 | 9.52 | 9.1 |
| B9 | 10.43 | 10.3 |
| B48 | 14.52 | 13.8 |
| B28 | 16.81 | 17.2 |

## References

[1] A.B. Spierings, M. Schneider, R. Eggenberger, Comparison of density measurement techniques for additive manufactured metallic parts, Rapid Prototyp. J. vol. 17 (5) (2011) 380–386, https://doi.org/10.1108/13552541111156504.

[2] T. de Terris, et al., Optimization and comparison of porosity rate measurement methods of selective laser melted metallic parts, Addit. Manuf. vol. 28 (2019) 802–813, https://doi.org/10.1016/j.addma.2019.05.035.

[3] B. Westman, et al., Analysis and comparison of focused ion beam milling and vibratory polishing sample surface preparation methods for porosity study of U-Mo plate fuel for research and test reactors, Micron vol. 110 (2018) 57–66, https://doi.org/10.1016/j.micron.2018.04.010.

[4] L. De Chiffre, S. Carmignato, J.-P. Kruth, R. Schmitt, A. Weckenmann, Industrial applications of computed tomography, CIRP Ann. vol. 63 (2) (2014) 655–677.

[5] J.P. Kruth, M. Bartscher, S. Carmignato, R. Schmitt, L. De Chiffre, A. Weckenmann, Computed tomography for dimensional metrology, CIRP Ann. vol. 60 (2) (2011) 821–842.

[6] W.W. Wits, S. Carmignato, F. Zanini, T.H.J. Vaneker, Porosity testing methods for the quality assessment of selective laser melted parts, CIRP Ann. vol. 65 (1) (2016) 201–204, https://doi.org/10.1016/j.cirp.2016.04.054.

[7] A. Migliori, et al., Resonant ultrasound spectroscopic techniques for measurement of the elastic moduli of solids, Phys. B: Condens. Matter vol. 183 (1–2) (1993) 1–24, https://doi.org/10.1016/0921-4526(93)90048-B.

[8] F.F. Balakirev, S.M. Ennaceur, R.J. Migliori, B. Maiorov, A. Migliori, Resonant ultrasound spectroscopy: the essential toolbox, Rev. Sci. Instrum. vol. 90 (12) (2019), 121401, https://doi.org/10.1063/1.5123165.

[9] K. Flynn, M. Radovic, Evaluation of defects in materials using resonant ultrasound spectroscopy, J. Mater. Sci. vol. 46 (8) (2011) 2548–2556, https://doi.org/10.1007/s10853-010-5107-y.

[10] A. Belyaev, O. Polupan, S. Ostapenko, D. Hess, J.P. Kalejs, Resonance ultrasonic vibration diagnostics of elastic stress in full-size silicon wafers, Semicond. Sci. Technol. vol. 21 (3) (2006) 254–260, https://doi.org/10.1088/0268-1242/21/3/007.

[11] A. Belyaev, O. Polupan, W. Dallas, S. Ostapenko, D. Hess, J. Wohlgemuth, Crack detection and analyses using resonance ultrasonic vibrations in full-size crystalline silicon wafers, Appl. Phys. Lett. vol. 88 (11) (2006), 111907, https://doi.org/10.1063/1.2186393.

[12] M. Janovská, P. Sedlák, J. Cizek, M. Koller, F. Šiška, H. Seiner, Characterization of bonding quality of a cold-sprayed deposit by laser resonant ultrasound spectroscopy, Ultrasonics vol. 106 (2020), 106140, https://doi.org/10.1016/j.ultras.2020.106140.

[13] J.D. Trolinger, A. Lal, A. Dioumaev, D. Dimas, A non-destructive evaluation system for additive manufacturing based on acoustic signature analysis with laser Doppler vibrometry, Interferom. XIX, San. Diego, U. S. (2018) 12, https://doi.org/10.1117/12.2320445.

[14] J. Rossin, et al., Assessment of grain structure evolution with resonant ultrasound spectroscopy in additively manufactured nickel alloys, Mater. Charact. vol. 167 (2020), 110501, https://doi.org/10.1016/j.matchar.2020.110501.

[15] S. McGuigan, A.P. Arguelles, A.-F. Obaton, A.M. Donmez, J. Riviere, P. Shokouhi, Resonant ultrasound spectroscopy for quality control of geometrically complex additively manufactured components, Addit. Manuf. vol. 39 (2021), 101808, https://doi.org/10.1016/j.addma.2020.101808.

[16] J. Rossin, et al., Bayesian inference of elastic constants and texture coefficients in additively manufactured cobalt-nickel superalloys using resonant ultrasound spectroscopy, Acta Mater. vol. 220 (2021), 117287, https://doi.org/10.1016/j.actamat.2021.117287.

[17] M. Opprecht, J.-P. Garandet, G. Roux, C. Flament, An understanding of duplex microstructures encountered during high strength aluminium alloy laser beam melting processing, Acta Mater. vol. 215 (2021), 117024, https://doi.org/10.1016/j.actamat.2021.117024.

[18] B.J. Zadler, J.H. Le Rousseau, J.A. Scales, M.L. Smith, Resonant ultrasound spectroscopy: theory and application, Geophys. J. Int. vol. 156 (1) (2004) 154–169.

[19] M. Newville, T. Stensitzki, D.B. Allen, A. Ingargiola, LMFIT: non-linear least-square minimization and curve-fitting for python, Zenodo (2014), https://doi.org/10.5281/zenodo.11813.

[20] P. Virtanen, et al., SciPy 1.0: fundamental algorithms for scientific computing in python, Nat. Methods vol. 17 (3) (2020), https://doi.org/10.1038/s41592-019-0686-2. Art. no. 3.

[21] J. Nejezchlebová, H. Seiner, M. Ševčík, M. Landa, M. Karlík, Ultrasonic detection of ductile-to-brittle transitions in free-cutting aluminum alloys, NDT E Int. vol. 69 (2015) 40–47, https://doi.org/10.1016/j.ndteint.2014.09.007.

[22] J.A. Slotwinski, E.J. Garboczi, K.M. Hebenstreit, Porosity measurements and analysis for metal additive manufacturing process control, J. Res. Natl. Inst. Stand. vol. 119 (2014) 494, https://doi.org/10.6028/jres.119.019.

[23] N.V. Karthik, H. Gu, D. Pal, T. Starr, and B. Stucker, "High Frequency Ultrasonic Non Destructive Evaluation of Additively Manufactured Components," p. 15, 2013.

[24] P. Hermanek, J.S. Rathore, V. Aloisi, S. Carmignato, Principles of X-ray computed tomography, in: S. Carmignato, W. Dewulf, R. Leach (Eds.), in Industrial X-Ray

Computed Tomography, Springer International Publishing, Cham, 2018, pp. 25–67, https://doi.org/10.1007/978-3-319-59573-3_2.
[25] J.S. Rathore, C. Vienne, Y. Quinsat, C. Tournier, Influence of resolution on the X-ray CT-based measurements of metallic AM lattice structures, Weld. World vol. 64 (2020) 1367–1376.
[26] J.S. Rathore, C. Mang, C. Vienne, Y. Quinsat, C. Tournier, A methodology for computed tomography-based non-destructive geometrical evaluations of lattice structures by holistic strut measurement approach, J. Manuf. Sci. Eng. vol. 143 (5) (2021), 051012.
[27] M.C. Sow, et al., Influence of beam diameter on laser powder bed fusion (L-PBF) process, Addit. Manuf. vol. 36 (2020), 101532, https://doi.org/10.1016/j.addma.2020.101532.
[28] GE Additive, "AlSi7Mg data sheet," Nov. 2019. ⟨https://www.ge.com/additive/sites/default/files/2019–11/AlSi7Mg-M2beide.pdf⟩ (accessed Mar. 23, 2022).
[29] K. Miled, K. Sab, R. Le Roy, Effective elastic properties of porous materials: homogenization schemes vs experimental data, Mech. Res. Commun. vol. 38 (2) (2011) 131–135, https://doi.org/10.1016/j.mechrescom.2011.01.009.
[30] C. Kohlhauser, C. Hellmich, Determination of Poisson's ratios in isotropic, transversely isotropic, and orthotropic materials by means of combined ultrasonic-mechanical testing of normal stiffnesses: application to metals and wood, Eur. J. Mech. - A/Solids vol. 33 (2012) 82–98, https://doi.org/10.1016/j.euromechsol.2011.11.009.
[31] A. Khabouchi, P. Ventura, N. Leymarie, A. Hazotte, L. Germain, Crystallographic texture and velocities of ultrasonic waves in a Ni-based superalloy manufactured by laser powder bed fusion, Mater. Charact. vol. 169 (2020), 110607, https://doi.org/10.1016/j.matchar.2020.110607.
[32] M.I. Latypov, et al., Computational homogenization for multiscale forward modeling of resonant ultrasound spectroscopy of heterogeneous materials, Mater. Charact. vol. 158 (2019), 109945, https://doi.org/10.1016/j.matchar.2019.109945.
[33] J.A. Evans, et al., Determining elastic anisotropy of textured polycrystals using resonant ultrasound spectroscopy, J. Mater. Sci. vol. 56 (16) (. 2021) 10053–10073, https://doi.org/10.1007/s10853-021-05827-z.
[34] A. Migliori, J.L. Sarrao, Resonant Ultrasound Spectroscopy, John Wiley and Sons, 1997.
[35] H. Ogi, K. Sato, T. Asada, M. Hirao, Complete mode identification for resonance ultrasound spectroscopy, J. Acoust. Soc. Am. vol. 112 (6) (2002) 2553–2557, https://doi.org/10.1121/1.1512700.
[36] P. Sedlák, H. Seiner, J. Zídek, M. Janovská, M. Landa, Determination of all 21 independent elastic coefficients of generally anisotropic solids by resonant ultrasound spectroscopy: benchmark examples, Exp. Mech. vol. 54 (6) (2014) 1073–1085, https://doi.org/10.1007/s11340-014-9862-6.
[37] S. Bernard, G. Marrelec, P. Laugier, Q. Grimal, Bayesian normal modes identification and estimation of elastic coefficients in resonant ultrasound spectroscopy, Inverse Probl. vol. 31 (6) (2015), 065010.
[38] B.R. Goodlet, S.P. Murray, B. Bales, J. Rossin, C.J. Torbet, T.M. Pollock, Temperature dependence of single crystal elastic constants in a CoNi-Base alloy: a new methodology, Mater. Sci. Eng.: A (2020), 140507, https://doi.org/10.1016/j.msea.2020.140507.
[39] P. Van Cauwenbergh, et al., Unravelling the multi-scale structure–property relationship of laser powder bed fusion processed and heat-treated AlSi10Mg, Sci. Rep. vol. 11 (1) (2021) 6423, https://doi.org/10.1038/s41598-021-85047-2.